Ultra-durable Ni-Ir/MgAl2O4 catalysts for dry reforming of methane enabled by dynamic balance between carbon deposition and elimination

Haocheng Li
East China Normal University
Cong Hao
Xiamen University
Jingqing Tian
East China Normal University
Shuai Wang
Xiamen University https://orcid.org/0000-0002-4618-4162
Chen Zhao (czhao@chem.ecnu.edu.cn)
East China Normal University

Article

Keywords:

Posted Date: February 11th, 2022

DOI: https://doi.org/10.21203/rs.3.rs-1335282/v1

Ultra-durable Ni-Ir/$MgAl_2O_4$ catalysts for dry reforming of methane enabled by dynamic balance between carbon deposition and elimination

Abstract

Carbon deposition is the main cause for the catalyst deactivation of methane dry reforming, and researchers are committed to exploring effective catalyst systems with zero carbon deposition in order to achieve a practically long life-time. In this work, we propose an equilibrium theory with matched rates of CH_4 dissociation and CO_2 activation to establish a balance between carbon deposition and carbon elimination, and construct highly dispersed Ni-Ir/$MgAl_2O_4$ alloy catalysts accordingly, where Ni activated CH_4, $MgAl_2O_4$ adsorbed CO_2 to form surface carbonates, and Ir effectively utilized the carbonates to eliminate carbon species generated by CH_4 dissociation. Theoretical assessment further unveiled that the preferred CO_2 activation on Ir over Ni is derived from its stronger oxophilicity. With an optimal Ni/Ir atomic ratio of 1/2, high activity and long-period stability (600 h) with zero carbon deposition were obtained concurrently for dry reforming of methane at industrially-relevant temperature (650 °C).

Introduction

Dry reforming of methane (DRM) is a primary method for producing syngas (a mixture of CO and H_2) that acts as a key platform for the industrial production of fuels and chemicals [1-5]. Among group VIII metals [6-10], low-cost Ni has drawn the most attention for DRM because of its strong CH_4 dissociation ability, which endows Ni with an excellent catalytic performance of DRM [11-15]. However, Ni-based catalysts suffer from serious carbon deposition and metal sintering issues under the high-temperature condition of DRM (700-1000 °C), which limits their large-scale application [16-20]. The main causes of carbon deposition include the disproportionation of carbon monoxide ($2\ CO(g) \rightleftharpoons C(s) + CO_2(g)$; $\Delta H = -171$ kJ/mol) and the deep dissociation of methane ($CH_4(g) \rightleftharpoons C(s) + 2\ H_2(g)$; $\Delta H = 75$ kJ/mol), while the latter prevails at temperatures above 600 °C [21].

Various methods have been attempted to suppress the carbon deposits in DRM. By using supports rich in oxygen vacancies such as CeO_2 [22-24] or alkaline oxide supports like MgO [25-26], CO_2 activation can be strengthened to accelerate the elimination of carbon deposits. This enhances the redox property of the catalyst and inhibits the development of carbon deposition [27, 28]. The accumulation and sintering of metallic Ni at high temperatures (700-1000 °C) can result in the formation of larger Ni particles, which promotes the carbon deposition[29]. The strong metal-support interaction (SMSI) between metallic Ni and the hydroxyapatite [$Ca_{10}(PO_4)_6(OH)_2$] (HAP) support[30] was found to enhance the dispersion of Ni particles and alleviate sintering and carbon deposits concurrently. In addition, it was reported that decorating the Ni surface with Co prevented the continuous formation of carbon nanotubes on the Ni surface[31]. The redox recycling on Ni-Fe/$Mg_xAl_yO_z$ catalysts, where metallic Fe was oxidized by CO_2 to form FeO_x and the adsorbed C atom obtained from the dissociation of CH_4 reduced FeO_x back to Fe, can effectively eliminate carbon deposits [32]. Ni-Mo nanoparticles were stabilized on the edge of a single MgO crystal to inhibit the particle sintering at high temperatures and effectively prevent the generation of carbon deposits over a long reaction period (850 h) [33].

The core issue for achieving practically-durable DRM catalysts with minimal carbon deposition is to establish an efficient equilibrium between CH_4 dissociation and CO_2 activation on the catalyst surface. In this work, we show that a highly efficient and stable DRM system can be built on bimetallic Ni-Ir/$MgAl_2O_4$ catalysts, brought forth by a synergy between the CH_4 dissociation on Ni sites and $MgAl_2O_4$-enhanced CO_2 adsorption and activation on Ir sites that can scavenge surface carbon species generated from the CH_4 dissociation step. Through in-situ spectroscopic characterization of the generation and elimination of carbon species and theoretical calculations on the CO_2 activation, we propose an equilibrium mechanism of carbon generation and elimination for designing the effective and durable catalysts for the DRM process.

Results and discussion

Structural characterization of supported Ni-Ir catalysts

$MgAl_2O_4$-supported Ni, Ni_3Ir_1, and Ir catalysts were synthesized using a conventional co-impregnation method, and the surface areas of these catalysts were 126.0, 133.9, and 136.1 m^2/g, respectively, as determined by nitrogen physical adsorption (Fig. S1). X-ray diffraction (XRD) results (Fig. 1a) showed that the diffraction peaks of metallic Ni for $Ni_3Ir_1/MgAl_2O_4$ had a much lower intensity compared to the pure Ni catalyst. Similarly, compared with the pure Ir catalyst, the diffraction peaks of Ir had a lower intensity for $Ni_3Ir_1/MgAl_2O_4$. Such weakened diffraction peaks for the Ni-Ir catalyst implies that the interaction of Ni and Ir increased metal dispersion compared to the single-metal catalyst system. The Ni-Ir interaction is further evidenced by a shift of the signal peaks of metallic Ir in the presence of Ni (e.g., from 40.46° to 40.92° for the Ir(111) plane and from 47.12° to 47.66° for the Ir (200) plane, Fig. S2), consistent with the smaller atomic radius of Ni than Ir.

As shown in XPS profiles of Fig. 1b, the Ni^0 $2p_{3/2}$ (855.2 eV) and Ni^{2+} $2p_{3/2}$ (858.2 eV) signals were observed for the Ni/$MgAl_2O_4$ catalyst. The presence of Ni^{2+} cations indicates the formation of $NiAl_2O_4$ species on the support surface during the synthesis process. Compared with Ni/$MgAl_2O_4$, the Ni^{2+} content and binding energy position in the $Ni_3Ir_1/MgAl_2O_4$ catalyst changed minimally, while the Ni^0 $2p_{3/2}$ signal increased to 858.6 eV (by 0.4 eV). In contrast, the binding energy of Ir^0 $4f_{2/7}$ was 62.2 eV for the pure Ir catalyst (Fig. 1c), 0.4 eV higher than that in the Ni_3Ir_1 catalyst (61.8 eV). With respect to the monometallic Ni and Ir catalysts, these binding energy changes indicate the electrons were transferred from Ni to Ir, suggesting the formation of Ni-Ir alloy in the Ni-Ir/$MgAl_2O_4$ system. Ni and Ir K-edge X-ray adsorption fine structure (XAFS) spectroscopy was also used to identify the localized structure of the Ni-Ir alloy (Fig. S3, Table S1), which shows the existence of Ni-Ir coordination bonds (2.63–2.65 Å) in the $Ni_3Ir_1/MgAl_2O_4$ catalyst.

The structural information for the $Ni_3Ir_1/MgAl_2O_4$ catalyst was further confirmed by transmission electron microscopy (TEM) and energy dispersive spectroscopy (EDS) elemental mapping (Figs. 1d–g). The metal nanoparticles were uniformly dispersed on the $MgAl_2O_4$ spinel support surface with a typical bimodal particle size distribution, for which the corresponding average particle diameters were 1.2 and 4.3 nm and the smaller particles were predominant. In contrast, the average diameters of metal particles for Ir/$MgAl_2O_4$ and Ni/$MgAl_2O_4$ were 1.1 and 5.7 nm, respectively (Fig. S4). It is clearly indicated that the formation of the Ni-Ir alloy improved the dispersion of Ni, consistent with the XRD results shown above (Fig. 1a). In addition, the EDS analysis (Fig. 1e) showed that the small particles in the $Ni_3Ir_1/MgAl_2O_4$ catalyst possessed a higher content of Ir (Ni/Ir $\approx$ 2/3), while Ni dominated in the large particles (Ni/Ir $\approx$ 4/1). The uniform distributions of the Ni and Ir elements within each kind of the Ni-Ir particles (Figs. 1f–g, S5) agree well with the formation of alloys in the Ni-Ir/$MgAl_2O_4$ catalyst. Taken together, XRD, XPS, XAFS, TEM, and EDS were combined to verify that Ni-Ir alloys were formed in the bimetallic Ni-Ir/$MgAl_2O_4$ system, which significantly improved the dispersion of the Ni nanoparticles on the $MgAl_2O_4$ support and provided a basis for the efficient coupling between CH_4 dissociation and CO_2 activation on the Ni and Ir active sites, respectively, as demonstrated next for DRM.

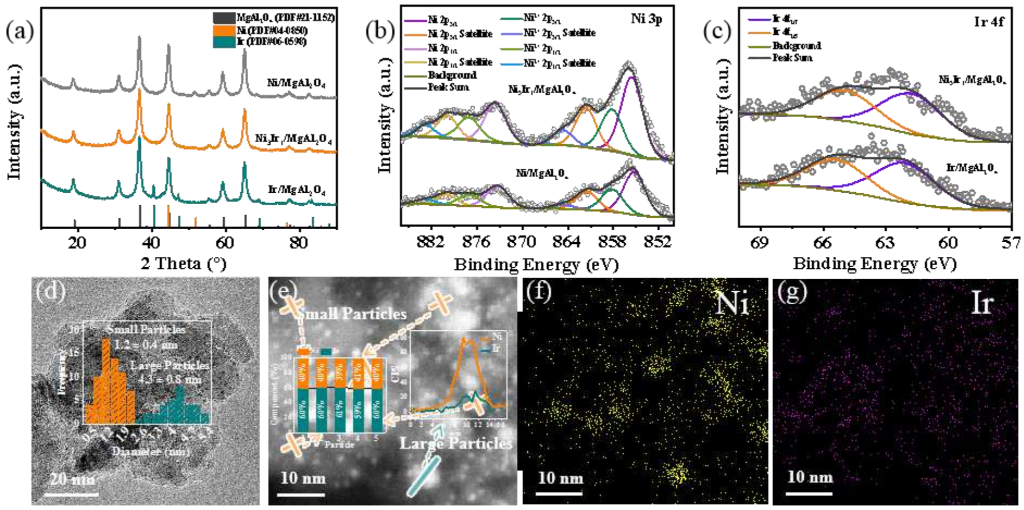

Fig. 1 (a) XRD patterns of Ni/MgAl$_2$O$_4$, Ni-Ir/MgAl$_2$O$_4$, and Ir/MgAl$_2$O$_4$, (b) Ni 3p XPS patterns of Ni/MgAl$_2$O$_4$ and Ni$_3$Ir$_1$/MgAl$_2$O$_4$, (c) Ir 4f XPS patterns of Ni$_3$Ir$_1$/MgAl$_2$O$_4$ and Ir/MgAl$_2$O$_4$, (d) HRTEM and particle size distribution of the metal nanoparticles, (e) EDS, and (f–g) EDS-mapping of Ni$_3$Ir$_1$/MgAl$_2$O$_4$.

Catalytic performances of Ni-Ir catalysts in DRM

From the view of thermodynamics, the DRM process is favorable at high temperatures due to its endothermic nature. At medium to low temperatures (below 700 °C), the impact of carbon deposits will be significant. The results for the Ni/MgAl$_2$O$_4$, Ni$_3$Ir$_1$/MgAl$_2$O$_4$, and Ir/MgAl$_2$O$_4$ catalysts are shown in Figs. 2a and S6 (650 °C, GHSV = 40,000 mL·g^{-1}·h^{-1}, 1 bar). For the pure Ni catalyst, the initial conversion of CH_4 was 59.4% and decreased to 47.3% after 100 hours of testing, in which the corresponding conversion of CO_2 decreased from 71.5% to 61.6%. It is reflected that the Ni catalyst was not able to maintain a good stability during DRM, although its initial activity was high. For the Ir catalyst, the initial conversions of CH_4 and CO_2 were only 50.2% and 63.6%, respectively, but the catalyst activity did not decrease significantly during the 100-hour test. For the Ni$_3$Ir$_1$/MgAl$_2$O$_4$ catalysts, the conversions of CH_4 and CO_2 slightly decreased from 61.5% to 60.2% and 73.3% to 72.8% during the 100-hour test, respectively, indicating the Ni-Ir alloy catalyst possessed both of high activity and improved stability. As shown in Table S2, we summarize the typical catalyst systems for DRM, and the Ni-Ir/MgAl$_2$O$_4$ system developed in our study had superior conversion rates of CH_4 and CO_2 than the state-of-the-art catalysts [9, 34-41].

For the DRM test with different temperatures (600–800 °C, Fig. S7), the initial conversion of CH_4 on the Ni, Ni_3Ir_1 and Ir catalysts increased with increasing temperature from 42.1%, 46.8%, and 20.9% at 600 °C to 89.8%, 90.4%, and 90.2% at 800 °C, respectively. Although the three catalysts showed significant differences in activity at the lower temperature, the gap decreased as the temperature increased until the activity was almost identical at 800 °C. The ratio of H_2/CO in the syngas showed a similar phenomenon, increasing from 0.67, 0.80, and 0.60 at 600°C to 0.96, 0.97, and 0.94 at 800 °C. It is suggested that DRM is preferred over the reverse water-gas shift reaction (RWGS; $CO_2 + H_2 \rightarrow CO + H_2O$) at temperatures above 600 °C, which leads to an increase in the H_2/CO ratio and gradually approaches unity as the temperature rises.

The different performances of the three catalysts in DRM may be directly related to their intrinsic abilities for the adsorption and activation of the CH_4 and CO_2 reactants. Kinetic studies (Figs. 2e–f) showed that the measured reaction order of CO_2 for Ni/$MgAl_2O_4$ was 0.12, while for Ni_3Ir_1/$MgAl_2O_4$ and Ir/$MgAl_2O_4$, the reaction order values were −0.13 and −0.57, respectively. These data indicate the adsorption strength of CO_2 on the three catalysts decreased with an order of Ir/$MgAl_2O_4$, Ni_3Ir_1/$MgAl_2O_4$, and Ni/$MgAl_2O_4$. As shown below, DFT calculations unveil that the higher oxophilicity of Ir than Ni accounts for the stronger CO_2 adsorption on Ir/$MgAl_2O_4$.

The measured reaction orders for CH_4 over the Ni, Ni_3Ir_1, and Ir catalysts were −0.38, −0.50, and −1.14, respectively, indicating the dissociative adsorption of CH_4 on Ir/$MgAl_2O_4$ was also the strongest among the three catalysts. This outstanding adsorption ability of Ir made it difficult for the reactive species to desorb from the catalyst surface, which limited the catalytic activity at medium to low temperatures. As the temperature increased, the desorption of the reactive species became easier and the catalytic activity of Ir/$MgAl_2O_4$ increased faster compared with the other two catalysts as evidenced by the changes of CH_4 conversion with increasing temperature (Fig. S7).

Characterization of spent Ni-Ir catalysts

It is generally accepted that carbon deposition is one of the main causes of catalyst deactivation in DRM [16,18]. SEM images (Figs. 2b–d) of the spent catalysts clearly showed the appearance of carbon deposits after the DRM reaction, which were interlaced and attached to the catalyst surface, blocking contact between the active metal site and the reactants and thus inhibiting the catalytic activity. Specifically, Ni/$MgAl_2O_4$ had more carbon deposits than Ni_3Ir_1/$MgAl_2O_4$, and the carbon chains on Ni/$MgAl_2O_4$ were longer and thicker than the latter, with average diameters of about 27.9 nm versus 21.5 nm. The carbon deposits also showed different morphologies for each catalyst, presumably due to the different amount of carbon species provided for the carbon chain growth for each catalyst. It is worth noting that the carbon deposition was nearly negligible on the Ir catalyst (Fig. 2d), consistent with the high stability of this catalyst for DRM.

XRD patterns of the spent Ni/$MgAl_2O_4$ catalyst showed an obvious graphite-2H signal (2θ = 25.9°), which is typical of amorphous carbon species produced in DRM (Fig. 2g). The intensity of the graphite-2H signal for Ni_3Ir_1 was lower than that for Ni, while this signal was not detectable on the Ir catalyst. Raman spectra of these spent catalysts (Fig. 2h) showed peaks at 1334 and 1598 cm^{-1} for both Ni and Ni_3Ir_1, which were assigned to the D-band and G-band signals of carbon species. Although the peak intensity of Ni was higher, the peak intensity ratios of the D-band and G-band signals were similar between the two catalysts, indicating no significant differences in the types of carbon deposits formed. For the spent Ir catalyst, no corresponding peaks were observed, consistent with the XRD characterization. To quantify the amount of carbon deposits formed on the spent catalysts, TGA analysis was conducted (Fig. 2i). No significant weight loss was observed for the Ir catalyst during the TGA process, while the Ni and Ni_3Ir_1 catalysts showed weight losses of 16.7% and 10.2%, respectively. These data unambiguously reflect that the addition of Ir suppressed the formation of carbon deposits in DRM.

TEM characterization was further applied to analyze the structure and morphology of the spent catalysts after long-time reaction (Fig. S8). The average diameter of the Ni nanoparticles on Ni/$MgAl_2O_4$ increased from 5.7 to 8.2 nm (5.7 nm for the fresh sample) after 100 hours of testing, indicative a severe sintering of the Ni particles at the condition of DRM. In contrast, the metal particle sizes of the spent Ni_3Ir_1 and Ir catalysts (1.2 and 4.1 nm for Ni_3Ir_1/$MgAl_2O_4$; 1.1 nm for Ir/$MgAl_2O_4$) did not change significantly compared with the fresh ones. It is surmised that metallic Ir has a strong interaction with the $MgAl_2O_4$ support, which results in the smaller metal particles and stronger anti-sintering ability for the Ir-containing catalysts.

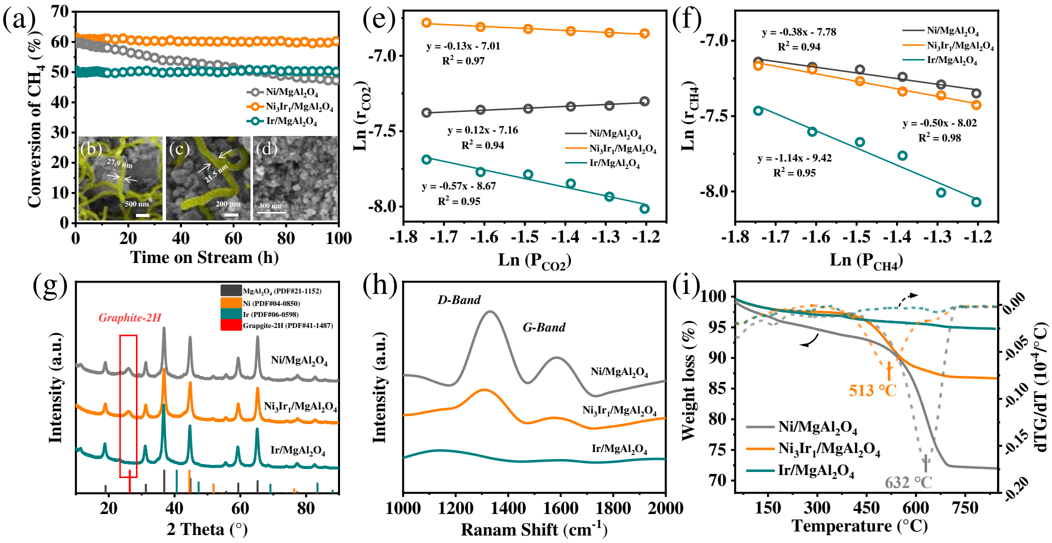

Fig. 2 (a) CH_4 conversion on Ni/$MgAl_2O_4$, Ni_3Ir_1/$MgAl_2O_4$, and Ir/$MgAl_2O_4$ (reaction conditions for the catalytic test: 650 °C, CH_4/CO_2=1/1, GHSV = 40,000 $mL\cdot g^{-1}\cdot h^{-1}$, and 1 bar); (e-f) kinetic analysis; (b-d) SEM images, (g) XRD patterns, (h) Raman spectra, (i) TGA, and of the spent catalysts.

In-situ DRIFTS study of DRM

Adsorption of CO_2 on the $MgAl_2O_4$ support can form carbonate species, which may promote the fixation and activation of CO_2 during the DRM. In-situ diffuse reflectance infrared fourier transform spectroscopy (DRIFTS) analysis showed that $MgAl_2O_4$ adsorbed CO_2 and converted it into carbonate species readily at 650 °C in a CO_2 atmosphere (Fig. S9a). TGA was further performed to assess the CO_2 adsorption capacity of $MgAl_2O_4$ (Fig. S9b), which was approximately 1.0 wt% at 650 °C. As the temperature decreased, the adsorption capacity of $MgAl_2O_4$ continued to increase, and reached about 2.6 wt% at 50 °C. Although the adsorption capacity was not significant at high temperatures, the adsorption and desorption of CO_2 occurred simultaneously during the DRM process and could dynamically provide CO_2 for the active metal sites, beneficial for the capture and utilization of gaseous CO_2.

To further ascertain the specific impact of carbonates on $MgAl_2O_4$ for DRM, in-situ DRIFTS was employed to analyze the activation process through the step-by-step introduction of CO_2-CH_4-CO_2 atmosphere. Within the first minute of introducing CO_2, all the three catalysts showed vibrational peaks at 1643 and 1542 cm^{-1} (attributed to monodentate carbonate species [42-43]), indicating all the catalysts can adsorb CO_2 to form carbonate (Fig. S10). Subsequently, the IR reactor cell was purged with Ar, and CH_4 was introduced in the second stage. The in-situ DRIFTS spectra for the three catalysts during the CH_4 stage are shown in Figs. 3a–c; the carbonate signals slowly decreased over time and those for Ni/$MgAl_2O_4$ decreased faster than the other two catalysts. It is worth noting that, at the beginning of the CH_4 stage for Ni/$MgAl_2O_4$, the gaseous CO_2 signal initially increased and then slowly decreased; however, no gaseous CO_2 was detectable on the other two catalysts. In addition, all the catalysts were observed generating CO (twin peak at 2150 cm^{-1}), and the generation rate of CO was relatively slow on the Ni/$MgAl_2O_4$ catalyst, with a noticeable CO signal observed only after 1 minute of introducing CH_4, while the other catalysts showed obvious CO formation upon the initiation of the stage.

In the third stage, we again used Ar to purge the residual CH_4 and then reintroduced CO_2. The in-situ DRIFTS spectra of the catalysts during this stage again showed that carbonate species were formed on the catalysts (Figs. 3d–f). This occurred more slowly on the Ni/$MgAl_2O_4$ catalyst, requiring 2.5 minutes to reach carbonate species saturation while on the other two catalysts, the saturation was reached after just 1 minute. Further, the signal peak for gaseous CO only appeared for the Ni_3Ir_1/$MgAl_2O_4$ catalyst.

Two distinct reaction pathways are proposed to explain the observed difference during the in-situ DRIFTS experiments described above. The Ni/$MgAl_2O_4$ catalyst followed reaction path A (Fig. 3g). Namely, when CO_2 was first introduced, the $MgAl_2O_4$ support adsorbed gaseous CO_2 and formed monodentate carbonate species

(CO_2 (g) → $CO_3^{2-}$$_{, ads}$), thus allowing the carbonate species to reach saturation. When CH_4 was introduced in the second stage, it was dissociated on the active metal sites, forming surface CH_x* (x = 0–3) species (CH_4 (g) → H* + CH_x*), which continued to accumulate and form carbon deposits. The carbonate species on $MgAl_2O_4$ cannot be used by the active Ni sites directly, while it can decompose into gaseous CO_2 ($CO_3^{2-}$$_{ads}$ → CO_2 (g)) again, which then adsorbed on the active Ni sites and further reacted with CH_x* to form CO* (CO_2* + CH_x* → 2CO (g) + x/2 H_2). CO* was finally released from the catalyst surface to form gaseous CO. Therefore, when CH_4 was introduced during the second stage, CO was not produced until sufficient carbonate was consumed to generate CO_2. Only easily eliminated carbon species were activated and removed by the reaction with CO_2 released by the support in the second stage, leaving the catalyst surface covered by the recalcitrant carbon chains produced by overgrowth. Since Ni could not effectively activate and utilize CO_2 to eliminate the carbon chains, when CO_2 was reintroduced in the third stage, only the accumulation of carbonate species on the support occurred without the formation of CO.

In contrast to Ni/$MgAl_2O_4$, the Ir/$MgAl_2O_4$ catalyst followed reaction path B (Fig. 3h). The difference was that the Ir active sites could directly use and activate the carbonate species on the support, eliminating the CH_x* and forming gaseous CO ($CO_3^{2-}$$_{, ads}$ + CH_x* → CO (g)). The carbonate species did not have to decompose into CO_2 (g) to be reused, therefore there was a large amount of CO formed without obvious CO_2 formation. The direct utilization of carbonate on the Ir based catalysts increased the utilization rate of carbonate species, resulting in a slower rate of consumption compared to route A. Compared with Ni, Ir had an insufficient ability to activate CH_4, therefore the carbonate species that adsorbed on the surface of $MgAl_2O_4$ in the first stage was sufficient to eliminate the CH_x* generated during the second stage, which resulted in no CO formation in the third stage. We also increased the time for CH_4 introduction in the second stage of the Ir/$MgAl_2O_4$ catalyst to ensure that enough CH_x* were generated. After CO_2 was introduced again, gaseous CO signals appeared indicating that the Ir/$MgAl_2O_4$ catalyst could reduce the carbon species and CO_2 to CO (Fig. S11).

The Ni_3Ir_1/$MgAl_2O_4$ catalyst also followed reaction path B. Due to the presence of Ni, the dissociation ability of CH_4 was better than the Ir/$MgAl_2O_4$ catalyst, therefore CH_x* species were not completely eliminated and grew into carbon chains in the second stage. In the third stage, gaseous CO formed in addition to the carbonate but was slower because the carbonate was not saturated during the initial stage of CO_2 introduction. With saturation of the carbonate species, the formation rate of gaseous CO increased accordingly, which further confirmed that carbonate was used as a bridge to adsorb and convert CO_2 rather than directly utilize gaseous CO_2. Both the Ni_3Ir_1/$MgAl_2O_4$ and Ni/$MgAl_2O_4$ catalysts generated carbon species, which grew into carbon chains in the second stage. However, in the third stage, only the Ni_3Ir_1/$MgAl_2O_4$ catalyst following path B eliminated the carbon species completely and formed gaseous CO. This suggests that path B was more beneficial to the activation of CO_2 and the elimination of carbon species.

To verify the unique roles of $MgAl_2O_4$ in the DRM, an Ir/Al_2O_3 catalyst was further characterized by the in-situ DRIFTS experiment (Fig. S12). When CO_2 was introduced in the first stage, no carbonate species formed and only obvious gaseous CO_2 signal peaks appeared. In the second stage, no gaseous CO signal peak appeared during the introduction of CH_4, because the carbon species were eliminated in a CH_4 atmosphere without carbonates formed on the support surface. The third stage was the same as the second stage, with no obvious gaseous CO signal peaks. Although carbon species were produced by the activation of CH_4 (TPSR-MS, in-situ DRIFTS) in the second stage, Ir weakly utilized gaseous CO_2 to eliminate carbon species, and only a small amount of carbon species which had not continued to grow was further activated, forming a small amount of CO. Therefore, only the Ir-CO signal (2000 cm^{-1}) was observed on the Ir catalyst, and the amount of gaseous CO did not reach the detection limit. This proves that the carbonate formed on the $MgAl_2O_4$ support played a key role in the effective removal of carbon by Ir during the DRM.

In order to further explore the adsorption and activation ability of CO_2 on different catalysts, the catalysts were characterized with temperature programmed desorption of CO_2 (CO_2-TPD) showed a signal peak appeared only at 614 °C on $MgAl_2O_4$, and the peak position of Ni/$MgAl_2O_4$ was similar to that of $MgAl_2O_4$, but with a lower intensity

(Fig. S13). For $Ni_3Ir_1/MgAl_2O_4$, in addition to a peak appeared at 621 °C (similar to the support), there were peaks at 778 and 873 °C, and the peaks at 621 °C and 809 °C were present for $Ir/MgAl_2O_4$. This was because Ir had better dispersion and CO_2 could be effectively adsorbed and utilized at the Ir-$MgAl_2O_4$ interface, while the Ni-$MgAl_2O_4$ interface has no effect on CO_2 adsorption. This further supports the findings from the kinetics studies and in-situ DRIFTS, which Ir sites impacted adsorption and activation of CO_2 and restricted carbon deposits during the DRM.

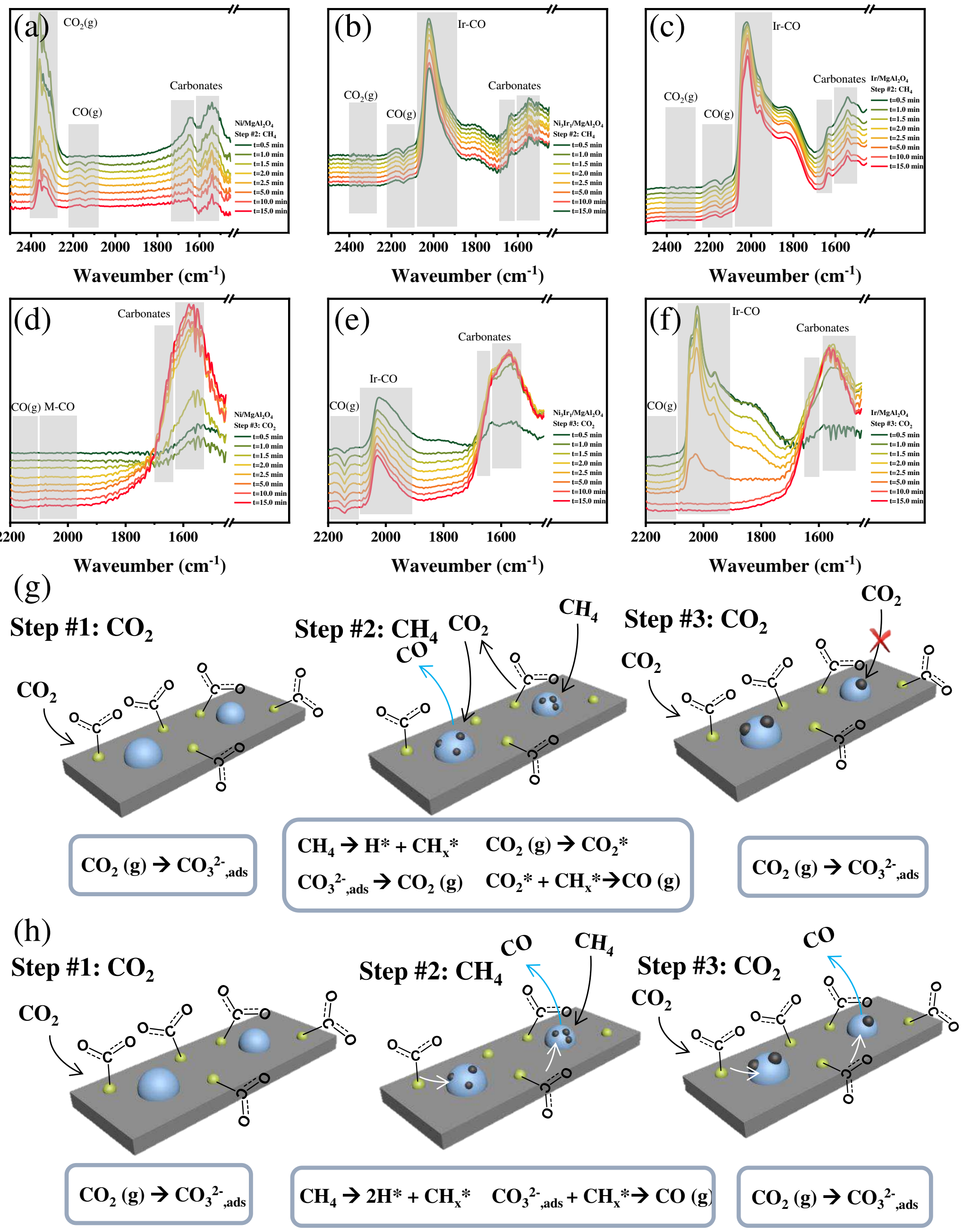

Fig. 3 In-situ DRIFTS with (a-c) introduction of CH_4 in the second stage, (d-f) introduction of CO_2 in the third stage of Ni/$MgAl_2O_4$, Ni_3Ir_1/$MgAl_2O_4$, Ir/$MgAl_2O_4$, the schematic diagram of the mechanism to activate CO_2 (g) with the help of carbonate and (h) without the help of carbonate.

TPSR-MS analysis of the activation of methane and the elimination of carbon deposits

The activation and dissociation of CH_4 is the main cause of carbon deposition during DRM. Temperature programmed surface reaction-mass (TPSR-MS) was used to explore the activation ability of CH_4 during the DRM process. First, CH_4 was introduced during the temperature-programming process (Figs. S14a and S15). The $Ni/MgAl_2O_4$, $Ni_3Ir_1/MgAl_2O_4$, and $Ir/MgAl_2O_4$ catalysts exhibited CH_4 activation abilities at 289, 328, and 347 °C, respectively. The carbon species generated by the dissociation of CH_4 blocked the active sites, restricting the activation of CH_4. This caused the CH_4 activation ability to decrease at 490, 610, and 590 °C, respectively. This indicates that Ni was better than Ir for dissociation of CH_4, and the dissociation rate increased with raising temperature.

Subsequently, TPSR-MS was performed on the catalysts after CH_4 treatment to explore how the different catalytic systems eliminate carbon deposits in a CO_2 atmosphere (Fig. S14b). Overall, the carbon removal temperature on $Ni/MgAl_2O_4$ was higher than that on $Ni_3Ir_1/MgAl_2O_4$ and $Ir/MgAl_2O_4$, which confirmed the $Ni_3Ir_1/MgAl_2O_4$ and $Ir/MgAl_2O_4$ catalysts had stronger carbon removal abilities. The $Ni/MgAl_2O_4$ catalyst had a relatively small amount of activated CH_4 due to the blockage of active sites at lower temperatures, and the amount of carbon deposits and the resulting peak area were both relatively small. The above results show that $Ni_3Ir_1/MgAl_2O_4$ and $Ir/MgAl_2O_4$ which followed path B had advantages in the process of activating CO_2 and removing carbon species.

Raman spectra of the catalysts treated with CH_4 showed that all of them had D-band and G-band carbon peaks (Fig. S16) and the carbon content followed Ni-Ir > Ir > Ni, which was consistent with the TPSR-MS-CO_2 results. In addition, the ratio of the D-band to the G-band indicated that the catalysts formed the same type of carbon species upon the dissociation of CH_4. The different temperatures for CO_2 removal reflect the difference in the activation mechanism of CO_2 as described in the previous section.

Theoretical assessment of CO_2 activation on supported metal catalyst

As shown above, the activation of CO_2 over metal surface is critical for the efficient removal of carbon deposits during DRM. DFT calculations were further performed to understand the difference between Ir and Ni on CO_2 activation at a molecular level. Herein, a Ni_8 cluster, a Ir_8 cluster, and two Ni_6Ir_2 clusters with distinct configurations (denoted as $Ni_6Ir_2/MgAl_2O_4$-a and $Ni_6Ir_2/MgAl_2O_4$-b) were constructed on a $MgAl_2O_4$ (100) surface for modeling the $Ir/MgAl_2O_4$, $Ni/MgAl_2O_4$ and $Ni_3Ir/MgAl_2O_4$ catalysts, respectively (Fig. 4a). Previous studies indicate that such M_8 (M = metal) clusters were sufficient to reflect the characteristic of supported metal nanoparticles. [44-45]

Considering that the elimination of carbon deposits during DRM mainly depends on the active O* species generated from CO_2 dissociation [46-50], we therefore focused on the adsorption and dissociation processes of CO_2 at the metal-support interface. As shown in Fig. 4b, CO_2 adsorption was much stronger on $Ir_8/MgAl_2O_4$ than $Ni_8/MgAl_2O_4$ (-2.14 eV vs -1.14 eV), consistent with the in-situ DRIFTS experiments. For $Ni_6Ir_2/MgAl_2O_4$, the adsorption energy of CO_2 was between those for the Ir_8 and Ni_8 clusters, no matter the C atom of the adsorbed CO_2 on the Ni_6Ir_2 clusters was bound to the Ni site (i.e., $Ni_6Ir_2/MgAl_2O_4$-a; -1.33 eV) or the Ir site (i.e., $Ni_6Ir_2/MgAl_2O_4$-b; -1.77 eV).

DFT calculations showed that the CO_2 dissociation ($CO_2^* \rightarrow CO^* + O^*$, Fig. 4b) at the $Ir_8/MgAl_2O_4$ interface was exothermic by -0.41 eV with an activation barrier of 1.48 eV, which was considerably lower than that on $Ni_8/MgAl_2O_4$ interface (2.18 eV). The difference of the activation barrier for CO_2 dissociation indicates, compared with the Ni_8 cluster, the generation of O* species on the Ir_8 cluster was much more efficient, rendering a fast elimination of carbon deposits and thus a high catalyst stability during DRM. For the two $Ni_6Ir_2/MgAl_2O_4$ models, CO_2 was dissociated on $Ni_6Ir_2/MgAl_2O_4$-a with the formed CO* species bound to a Ni site via a C-Ni coronation and the formed O* atom bound to a vicinal Ir site, while these two moieties formed on $Ni_6Ir_2/MgAl_2O_4$-b were bound to the Ni and Ir sites inversely. CO_2 dissociation on $Ni_6Ir_2/MgAl_2O_4$-a showed a much lower activation barrier than that for $Ni_6Ir_2/MgAl_2O_4$-b (1.69 vs. 2.21 eV, Fig. 4b), further reflecting different stabilities of the incipiently formed CO* and O* species at the transition state (TS) of CO_2 dissociation on the Ir and Ni sites (TS structures shown in Fig. S17).

In order to unveil the determining factors on the activity of CO_2 dissociation, adsorption energies for O atom and CO on the supported M_8 clusters were calculated independently to compare the stabilities of these two species on different metal sites. As shown in Fig. 4c, the CO_2 dissociation barrier presented a nearly linear correlation with the O adsorption energy, while no apparent correlation was observed between the CO_2 dissociation barrier and the CO adsorption energy. These data clearly imply that the activity of CO_2 dissociation is mainly determined by the stabilization of the O* species at the TS, which prefers the Ir site over the Ni site.

The projected density of states (DOS) distributions of adsorbed O and M_8 clusters were further analyzed (Fig. 4d) to obtain a deeper understanding of the higher oxygen affinity of Ir. It is found that the antibonding states of O_{2p} became more populated in the trend of $Ir_8/MgAl_2O_4$, $Ni_6Ir_2/MgAl_2O_4$-a, $Ni_8/MgAl_2O_4$ and $Ni_6Ir_2/MgAl_2O_4$-b, accounting for the decrease of the stability of the O* species and the increase of the CO_2 dissociation barrier with this trend. Accordingly, the excellent stability of $Ir/MgAl_2O_4$ and $Ni_3Ir/MgAl_2O_4$ catalysts during DRM is attributable to their stronger oxophilicity derived from metal Ir.

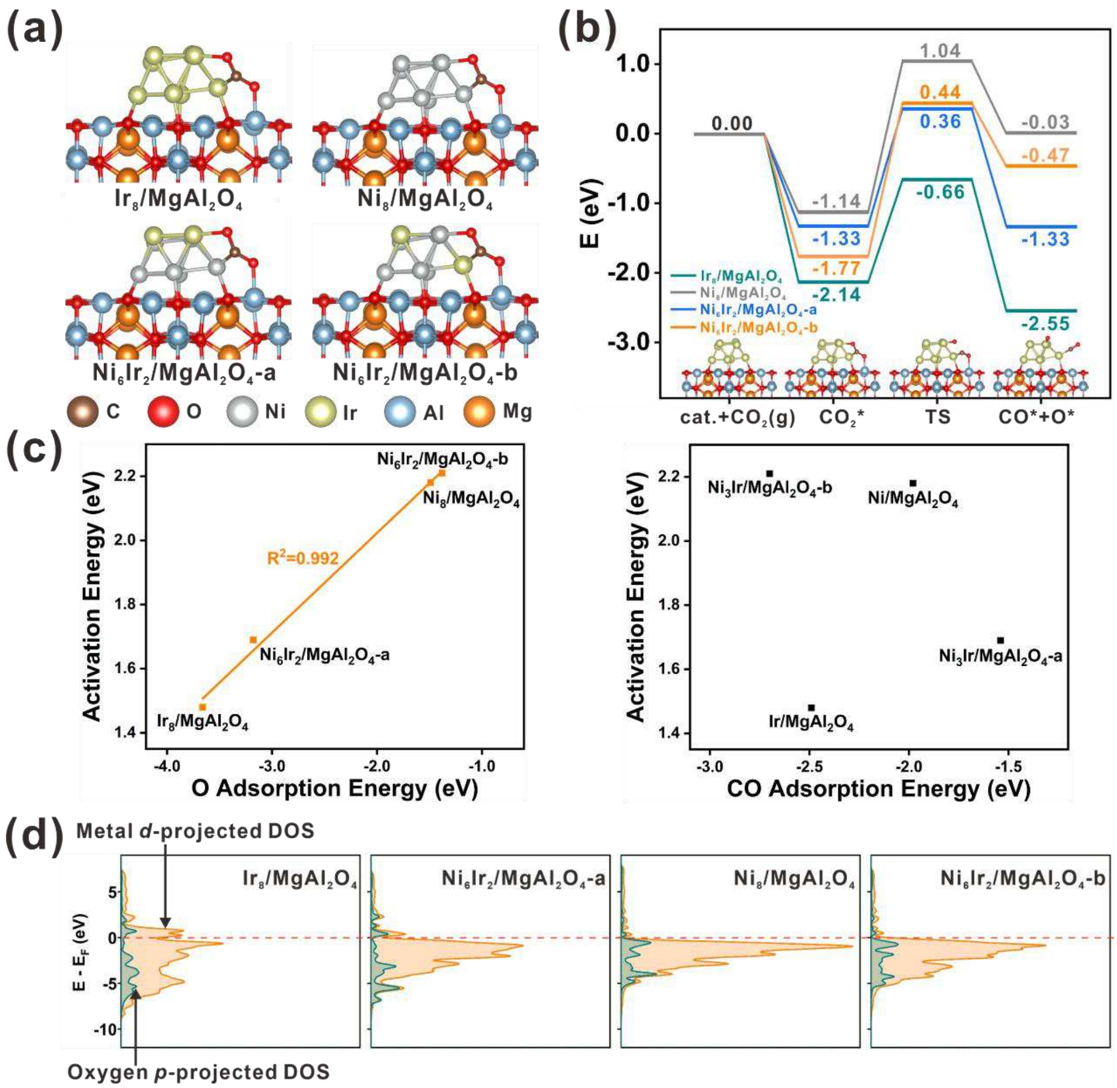

Fig. 4 (a) Four $M_8/MgAl_2O_4$ catalyst models applied in the theoretical calculations of DRM (with CO_2 adsorbed on the metal clusters). (b) DFT-derived energy changes of CO_2 dissociative adsorption on $M_8/MgAl_2O_4$. (c) Correlations of the CO_2 activation barrier with the adsorption energies of O-atom and CO on $M_8/MgAl_2O_4$. (d) Local density of states projected onto the adsorbed oxygen 2p state and M_8 cluster d state for the oxygen chemisorption on $M_8/MgAl_2O_4$.

Mechanism of carbon deposits-elimination balance in DRM and its application

With respect to the $Ni_3Ir_1/MgAl_2O_4$ catalyst, Ni mainly played the role of dissociating CH_4, while $MgAl_2O_4$ not only acted as the support of the active metal sites, but also adsorbed CO_2, forming carbonate species to enrich CO_2. These carbonate species could be effectively activated by Ir to eliminate carbon species and inhibit carbon deposition. Since the main activation sites of CH_4 and CO_2 were different (Ni for CH_4; Ir for CO_2), the ratios of Ni and Ir atoms can greatly modulate the activation rates of CH_4 and CO_2.

During the DRM process, although the Ni-Ir/$MgAl_2O_4$ system had more carbon deposits, it maintained high stability. Interestingly, the formed carbon deposits seemed to have no effect on the catalytic activity. Therefore, carbon deposits formed on the catalysts along with the reaction were examined (Fig. 5a). We found that Ni/$MgAl_2O_4$ had a faster rate of carbon deposition at the beginning and steadily increased. Further, as the carbon deposits increased, carbon chains blocked the contact between the active metal site and CH_4. The reduction in the amount of active sites for CH_4 dissociation led to a decrease in the rate of carbon deposition and DRM activity. In contrast, the Ir/$MgAl_2O_4$ catalyst did not form carbon deposits during the 100-hour test, while carbon deposits increased within the first 20 hours for Ni_3Ir_1/$MgAl_2O_4$, which was then stabilized with no significant additional increase until 100 hours.

Accordingly, we proposed a carbon deposits-elimination balance mechanism (Fig. 5b). With excessive Ni, the activation rate of CH_4 would be faster than that for CO_2, and the dissociated carbon species would not be eliminated in time, leading to the generation of carbon deposits. This type of carbon deposition occurred on Ni, the site activated by CH_4, which would block some of the Ni active sites. With a decrease in the Ni active sites, the activation rate of CH_4 decreased, resulting in a balance in the activation rate of CH_4 and CO_2. Similarly, excessive carbon deposits led to higher activation rates for CO_2 than CH_4, leading to the elimination of carbon deposits and exposing the Ni active sites previously covered. This caused the activation rate of CH_4 to increase until it matched that for CO_2 activation.

In the long-term test, this system gradually approached equilibrium until $\nu(CH_4) \approx \nu(CO_2)$ ($\nu(CH_4)$: the activation rate of CH_4; $\nu(CO_2)$: the activation rate of CO_2). This was also why numerous carbon deposits were observed in the Ni-Ir/$MgAl_2O_4$ catalytic system, but the effect on the catalytic activity was minimal. As $\nu(CH_4)$ approached $\nu(CO_2)$, the carbon deposits would no longer increase, but the existing carbon deposits would not be eliminated. In other words, the system achieved a balance between carbon deposition and elimination, and the overall reactivity was determined by the activation of CO_2. Over the Ni/$MgAl_2O_4$ catalyst, the dissociation of CH_4 and the activation of CO_2 occurred at the same active site, which did not follow this mechanism; thus, carbon deposits increased throughout the test. For the Ni_3Ir_1/$MgAl_2O_4$ catalyst, the Ni sites were reduced sufficiently such that the reaction system reached $\nu(CH_4) \approx \nu(CO_2)$ equilibrium after 20 hours.

Based on these results, Ni-Ir/$MgAl_2O_4$ catalysts were prepared with different Ni/Ir ratios for a 100-hour test to assess carbon deposition (Figs. 5c–d, S18-S19). With an increase in the Ir content from Ni/Ir = 12/1 to 1/3, the initial CH_4 conversion of the catalyst increased from 60.7% to 62.5%, and the average conversion of CH_4 increased from 59.1% to 62.4%. With increasing the Ir content, the activity and stability both increased. When the Ir/Ni ratio was 2, both of the initial and average conversions reached the highest level, and there was no further impact with an additional increase of the Ir content. In addition, the carbon deposits decreased from 14.2 wt% (Ni/Ir = 12/1) to 0 wt% (Ir/Ni = 2), and no carbon deposition occurred with further increasing the Ir content. This was because the increased Ir content brought more catalytic sites for CO_2 activation, allowing the system to reach the equilibrium between carbon deposition and elimination faster. Therefore, while maintaining high activity, the amount of carbon deposits was regularly reduced during the test. As the number of CO_2 activation sites increased, the activity of the rate-determining step in the reaction increased, and the system exhibited higher activity. This result was consistent with the balance theory, as when Ir/Ni = 2, $\nu(CO_2)$ matched $\nu(CH_4)$ during the initial stage of the test. Therefore, the carbon deposition was almost negligible, with almost no differences between the initial activity and the average activity of the reaction, indicating an extremely high stability of the catalytic system.

We anticipated that a match between $\nu(CO_2)$ and $\nu(CH_4)$ in the initial state of the reaction by tuning the Ni-Ir relative contents would achieve a balance between the generation and elimination of carbon deposits, leading to a DRM catalytic system with zero carbon deposits. Because Ir is a precious metal, it was necessary to reduce the Ir content as much as possible. As shown in Figs. 5c–d, the Ir/Ni ratio of 2 was found as the best catalyst ratio. We then conducted a 600 hours long-time test under the conditions of 650 °C, GHSV = 40,000 mL·g^{-1}·h^{-1}, and 1 bar (Fig. 5e). The initial conversion rates of CH_4 and CO_2 were 62.67 % and 72.94 %, respectively, with no significant change in activity after 600 hours. Raman spectra of the spent catalyst showed no obvious signal peaks for amorphous carbon at 1334 cm^{-1} or 1598 cm^{-1} (Fig. 5f). In addition, no significant weight loss was observed from TGA (Fig. 5g). These results confirmed that no obvious carbon deposition occurred on the catalyst, consistent with the results of the catalytic system optimized based on our proposed theory.

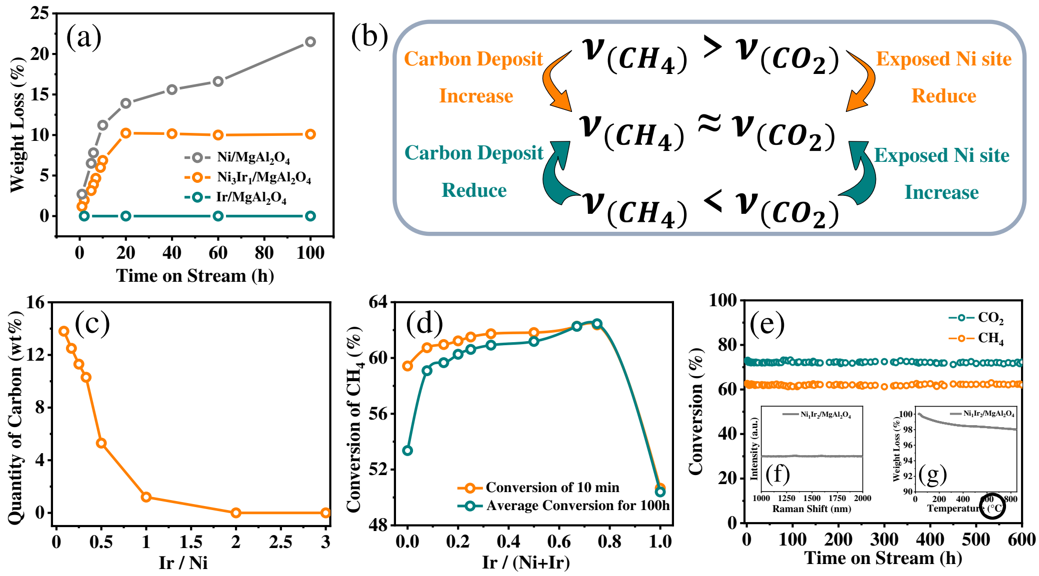

Fig. 5 (a) Relationship between carbon deposits and time on stream for $Ni/MgAl_2O_4$, $Ni_3Ir_1/MgAl_2O_4$, and $Ir/MgAl_2O_4$, (b) schematic diagram of the balance theory in DRM, (c) weight percent of carbon deposits from spent catalysts with varying Ir/Ni ratios, (d) relationship between the Ir content and catalytic activity, (e) catalytic performance during a long-term test of $Ni_1Ir_2/MgAl_2O_4$ for DRM, (f) Raman spectra, and (g) TGA of the spent catalysts after the long-term test of DRM.

Conclusions

Dry reforming of methane (DRM) to generate syngas can serve as a bridge for the high-volume utilization of greenhouse gases and synthesis of industrial platform molecules. The core of the stable DRM reaction is the equilibrium between efficient CH_4 dissociation and CO_2 activation. We designed and constructed an ultra-stable Ni-

Ir/$MgAl_2O_4$ alloy system for DRM showing high activity, where Ni played the role of activating CH_4 and $MgAl_2O_4$ adsorbed CO_2 to form carbonate species that can be effectively utilized by Ir to eliminate carbon species generated from CH_4 activation on Ni. Based on the feature of Ni, Ir and $MgAl_2O_4$, we proposed a balance mechanism between the active sites and the carbon deposits-eliminations over $Ni_1Ir_2/MgAl_2O_4$ catalytic system, which achieved equilibrium of $\nu(CH_4) \approx \nu(CO_2)$ at the beginning of the reaction, and effectively inhibited the generation of carbon deposits while maintaining high activity and stability. This deeper understanding of the relationship among the activity of CH_4 dissociation, CO_2 activation, and carbon deposition-elimination would inspire new ideas on the rational design and development of novel catalysts for activation of inert C_1 molecules.

References

1 Emiel de Smit, E. & Weckhuysen, B. M. The renaissance of iron-based Fischer-Tropsch synthesis: on the multifaceted catalyst deactivation behaviour. *Chem. Soc. Rev.* **37**, 2758-2781, doi:10.1039/b805427d (2008).

2 Xiong, H., Jewell, L. L. & Coville, N. J. Shaped Carbons As Supports for the Catalytic Conversion of Syngas to Clean Fuels. *ACS Catal.* **5**, 2640-2658, doi:10.1021/acscatal.5b00090 (2015).

3 Chen, Y. *et al.* Sintered precipitated iron catalysts with enhanced fragmentation-resistance ability for Fischer–Tropsch synthesis to lower olefins. *Catal. Sci. Technol.* **8**, 5943-5954, doi:10.1039/c8cy01392f (2018).

4 Chen, Y. *et al.* Ruthenium silica nanoreactors with varied metal–wall distance for efficient control of hydrocarbon distribution in Fischer–Tropsch synthesis. *J. Catal.* **365**, 429-439, doi:10.1016/j.jcat.2018.06.023 (2018).

5 Andrei Y. K., Wei C. & Pascal F. Advances in the Development of Novel Cobalt Fischer−Tropsch Catalysts for Synthesis of Long-Chain Hydrocarbons and Clean Fuels. *Chem. Rev.* **107**, 5, 1692-1744, doi:org/10.1021/cr050972v (2017).

6 Yentekakis, I. V. *et al.* Effect of support oxygen storage capacity on the catalytic performance of Rh nanoparticles for CO_2 reforming of methane. *Appl. Catal. B-Environ.* **243**, 490-501, doi:10.1016/j.apcatb.2018.10.048 (2019).

7 Zhang, Y. *et al.* Ru/TiO_2 Catalysts with Size-Dependent Metal/Support Interaction for Tunable Reactivity in Fischer–Tropsch Synthesis. *ACS Catal.* **10**, 12967-12975, doi:10.1021/acscatal.0c02780 (2020).

8 Zhang, J.-C. *et al.* Robust Ruthenium-Saving Catalyst for High-Temperature Carbon Dioxide Reforming of Methane. *ACS Catal.* **10**, 783-791, doi:10.1021/acscatal.9b03709 (2019).

9 Singha, R. K., Shukla, A., Sandupatla, A., Deo, G. & Bal, R. Synthesis and catalytic activity of a Pd doped Ni–MgO catalyst for dry reforming of methane. *J. Mater. Chem. A* **5**, 15688-15699, doi:10.1039/c7ta04452f (2017).

10 Kobayashi, T., Furuya, T., Fujitsuka, H. & Tago, T. Synthesis of Birdcage-type zeolite encapsulating ultrafine Pt nanoparticles and its application in dry reforming of methane. *Chem. Eng. J.* **377**, doi:10.1016/j.cej.2018.10.140 (2019).

11 Rodriguez, J. A., Grinter, D. C., Liu, Z., Palomino, R. M. & Senanayake, S. D. Ceria-based model catalysts: fundamental studies on the importance of the metal-ceria interface in CO oxidation, the water-gas shift, CO_2 hydrogenation, and methane and alcohol reforming. *Chem. Soc. Rev.* **46**, 1824-1841, doi:10.1039/c6cs00863a (2017).

12 Muraleedharan Nair, M. & Kaliaguine, S. Structured catalysts for dry reforming of methane. *New J. Chem.* **40**, 4049-4060, doi:10.1039/c5nj03268g (2016).

13 Li, S. & Gong, J. Strategies for improving the performance and stability of Ni-based catalysts for reforming reactions. *Chem. Soc. Rev.* **43**, 7245-7256, doi:10.1039/c4cs00223g (2014).

14 Tian, J., Ma, B., Bu, S., Yuan, Q. & Zhao, C. One-pot synthesis of highly sintering- and coking-resistant Ni nanoparticles encapsulated in dendritic mesoporous SiO_2 for methane dry reforming. *Chem. Commun. (Camb)* **54**, 13993-13996, doi:10.1039/c8cc08284g (2018).

15 Tian, J. *et al.* Facile immobilization of Ni nanoparticles into mesoporous MCM-41 channels for efficient methane dry reforming. *Chinese J. Catal.* **40**, 1395-1404, doi:10.1016/s1872-

2067(19)63403-0 (2019).

16 Pakhare, D. & Spivey, J. A review of dry (CO_2) reforming of methane over noble metal catalysts. *Chem. Soc. Rev.* **43**, 7813-7837, doi:10.1039/c3cs60395d (2014).

17 Ochoa, A. *et al.* Deactivation dynamics of a Ni supported catalyst during the steam reforming of volatiles from waste polyethylene pyrolysis. *Appl. Catal. B-Environ.* **209**, 554-565, doi:10.1016/j.apcatb.2017.02.015 (2017).

18 Lisiane V. M., Gary J., Burtron H. D. & Fábio B. N. Production of Hydrogen from Ethanol: Review of Reaction Mechanism and Catalyst Deactivation. *Chem. Rev.* **112**, 7, 4096-4123, doi: org/10.1021/cr2000114 (2012).

19 Saib, A. M. *et al.* Fundamental understanding of deactivation and regeneration of cobalt Fischer–Tropsch synthesis catalysts. *Catal. Today* **154**, 271-282, doi:10.1016/j.cattod.2010.02.008 (2010).

20 Tsakoumis, N. E., Rønning, M., Borg, Ø., Rytter, E. & Holmen, A. Deactivation of cobalt based Fischer–Tropsch catalysts: A review. *Catal. Today* **154**, 162-182, doi:10.1016/j.cattod.2010.02.077 (2010).

21 Wang, C. *et al.* Coking and deactivation of a mesoporous Ni–CaO–ZrO_2 catalyst in dry reforming of methane: A study under different feeding compositions. *Fuel* **143**, 527-535, doi:10.1016/j.fuel.2014.11.097 (2015).

22 Wang, F. *et al.* Enhanced catalytic performance of Ir catalysts supported on ceria-based solid solutions for methane dry reforming reaction. *Catal. Today* **281**, 295-303, doi:10.1016/j.cattod.2016.03.055 (2017).

23 Mortola VB, Damyanova S, Zanchet D, Bueno JMC. Surface and structural features of Pt/CeO_2-La_2O_3-Al_2O_3 catalysts for partial oxidation and steam reforming of methane. *Appl. Catal. B-Environ.* **107**, 221-236, doi: 10.1016/j.apcatb.2011.07.012 (2011).

24 Jeong D-W, Potdar HS, Shim J-O, Jang W-J, Roh H-S. H_2 production from a single stage water–gas shift reaction over Pt/CeO_2, Pt/ZrO_2, and Pt/$Ce_{(1-x)}Zr_{(x)}O_2$ catalysts. *Int. J. Hydrog. Energy* **38**, 4502-4507, doi: 10.1016/j.ijhydene.2013.01.200 (2013)

25 Alipour, Z., Rezaei, M. & Meshkani, F. Effect of Ni loadings on the activity and coke formation of MgO-modified Ni/Al_2O_3 nanocatalyst in dry reforming of methane. *J. Energy Chem.* **23**, 633-638, doi:10.1016/s2095-4956(14)60194-7 (2014).

26 Jabbour, K., Massiani, P., Davidson, A., Casale, S. & El Hassan, N. Ordered mesoporous "one-pot" synthesized Ni-Mg(Ca)-Al_2O_3 as effective and remarkably stable catalysts for combined steam and dry reforming of methane (CSDRM). *Appl. Catal. B-Environ.* **201**, 527-542, doi:10.1016/j.apcatb.2016.08.009 (2017).

27 Ay, H. & Üner, D. Dry reforming of methane over CeO_2 supported Ni, Co and Ni–Co catalysts. *Appl. Catal. B-Environ.* **179**, 128-138, doi:10.1016/j.apcatb.2015.05.013 (2015).

28 Faria, E. C., Neto, R. C. R., Colman, R. C. & Noronha, F. B. Hydrogen production through CO_2 reforming of methane over Ni/$CeZrO_2$/Al_2O_3 catalysts. *Catal. Today* **228**, 138-144, doi:10.1016/j.cattod.2013.10.058 (2014).

29 Jin-Hong Kim, Dong Jin Suh, Tae-Jin Park, Kyung-Lim Kim. Effect of metal particle size on coking during CO_2 reforming of CH_4 over Ni–alumina aerogel catalysts. *Appl. Catal. A-Gen.* **197**, 191-200, doi: 10.1016/S0926-860X(99)00487-1 (2000).

30 Kunitski, M. *et al.* Double-slit photoelectron interference in strong-field ionization of the neon dimer. *Nat. Commun.* **10**, 1, doi:10.1038/s41467-018-07882-8 (2019).

31 Cao, K. *et al.* Nickel catalyst with atomically-thin meshed cobalt coating for improved durability in dry reforming of methane. *J. Catal.* **373**, 351-360, doi:10.1016/j.jcat.2019.04.017 (2019).

32 Theofanidis, S. A., Galvita, V. V., Poelman, H. & Marin, G. B. Enhanced Carbon-Resistant Dry Reforming Fe-Ni Catalyst: Role of Fe. *ACS Catal.* **5**, 3028-3039, doi:10.1021/acscatal.5b00357 (2015).

33 Song Y. *et al.* Dry reforming of methane by stable Ni–Mo nanocatalysts on single-crystalline MgO. *Science* **367**, 777-781, doi: 10.1126/science.aav2412 (2020).

34 Pan, C., Guo, Z., Dai, H., Ren, R. & Chu, W. Anti-sintering mesoporous Ni-Pd bimetallic catalysts for hydrogen production via dry reforming of methane. *Int. J. Hydrog. Energy* **45**, 16133-16143, doi:10.1016/j.ijhydene.2020.04.066 (2020).

35 García-Diéguez, M., Pieta, I. S., Herrera, M. C., Larrubia, M. A. & Alemany, L. J. Nanostructured Pt- and Ni-based catalysts for CO_2-reforming of methane. *J. Catal.* **270**, 136-145, doi:10.1016/j.jcat.2009.12.010 (2010).

36 de Miguel, S. R. et al. Influence of Pt addition to Ni catalysts on the catalytic performance for long term dry reforming of methane. *Appl. Catal. A-Gen.* **435-436**, 10-18, doi:10.1016/j.apcata.2012.05.030 (2012).

37 Al-Fatesh, A. et al. Rh promoted and ZrO_2/Al_2O_3 supported Ni/Co based catalysts: High activity for CO_2 reforming, steam-CO_2 reforming and oxy-CO_2 reforming of CH_4. *Int. J. Hydrog. Energy* **43**, 12069-12080, doi:10.1016/j.ijhydene.2018.04.152 (2018).

38 Turap, Y. et al. Co–Ni alloy supported on CeO_2 as a bimetallic catalyst for dry reforming of methane. *Int. J. Hydrog. Energy* **45**, 6538-6548, doi:10.1016/j.ijhydene.2019.12.223 (2020).

39 Siang, T. J. et al. Hydrogen production from CH_4 dry reforming over bimetallic Ni-Co/Al_2O_3 catalyst. *J. Energy Inst*. **91**, 683-694, doi:10.1016/j.joei.2017.06.001 (2018).

40 Song, K. et al. Effect of alloy composition on catalytic performance and coke-resistance property of Ni-Cu/Mg(Al)O catalysts for dry reforming of methane. *Appl. Catal. B-Environ.* **239**, 324-333, doi:10.1016/j.apcatb.2018.08.023 (2018).

41 Al-Fatesh, A. S. Promotional effect of Gd over Ni/Y_2O_3 catalyst used in dry reforming of CH_4 for H_2 production. *Int. J. Hydrog. Energy* **42**, 18805-18816, doi:10.1016/j.ijhydene.2017.06.165 (2017).

42 Das S*, et al.* Effect of Partial Fe Substitution in $La_{0.9}Sr_{0.1}NiO_3$ Perovskite-Derived Catalysts on the Reaction Mechanism of Methane Dry Reforming. *ACS Catal.* **10**, 12466-12486 (2020).

43 Azancot L, Bobadilla LF, Centeno MA, Odriozola JA. IR spectroscopic insights into the coking-resistance effect of potassium on nickel-based catalyst during dry reforming of methane. *App. Catal. B-Environ.* **285**, (2021).

44 Cheng, F., Duan, X. & Xie, K. Dry reforming of methane by stable Ni nanocrystals on porous single-crystalline MgO monoliths at reduced temperature. *Angew. Chem. Int. Ed.* **60**, 18792-18799, doi:10.1002/anie.202106243 (2021).

45 Guo, Y.-P., Li, W.-Y. & Feng, J. Reaction pathway of CH_4/CO_2 reforming over Ni8/MgO(100). *Surf. Sci.* **660**, 22-30, doi:10.1016/j.susc.2017.02.010 (2017).

46 Akri, M. *et al.* Atomically dispersed nickel as coke-resistant active sites for methane dry reforming. *Nat. Commun.* **10**, 5181, doi:10.1038/s41467-019-12843-w (2019).

47 Wu, P. *et al.* Cooperation of Ni and CaO at interface for CO_2 reforming of CH_4: A combined theoretical and experimental study. *ACS Catal.* **9**, 10060-10069, doi:10.1021/acscatal.9b02286

(2019).

48 Tang, Y. *et al.* Synergy of single-atom Ni_1 and Ru_1 sites on CeO_2 for dry reforming of CH_4. *J. Am. Chem. Soc.* **141**, 7283-7293, doi: 10.1021/jacs.8b10910 (2019).

49 Joo, S. *et al.* Enhancing thermocatalytic activities by upshifting the d-band center of exsolved Co-Ni-Fe ternary alloy nanoparticles for the dry reforming of methane. *Angew. Chem. Int. Ed.* **60**, 15912-15919, doi:10.1002/anie.202101335 (2021).

50 Foppa, L. *et al.* Contrasting the role of Ni/Al2O3 interfaces in water-gas shift and dry reforming of methane. *J. Am. Chem. Soc.* **139**, 17128-17139, doi: 10.1021/jacs.7b08984 (2017).

Supplementary Files

This is a list of supplementary files associated with this preprint. Click to download.

- NiIrSIfinal.pdf